THE ASTRONOMICAL JOURNAL VOLUME 114, NUMBER 5 NOVEMBER 1997

DEEP INFRARED IMAGING OF THE R CORONAE AUSTRALIS CLOUD CORE

BRUCE A. WILKING
Department of Physics and Astronomy, University of Missouri–St. Louis, 8001 Natural Bridge Road, St. Louis, Missouri 63121
Electronic mail: brucew@newton.umsl.edu

MARK J. MCCAUGHREAN
Max-Planck-Institut für Radioastronomie, Auf dem Hügel 69, D-53121, Bonn, Germany
Electronic mail: mjm@mpifr-bonn.mpg.de

MICHAEL G. BURTON
School of Physics, University of New South Wales, Sydney, NSW 2052, Australia
Electronic mail: mgb@newt.phys.unsw.edu.au

TIMOTHY GIBLIN[1]
Department of Physics and Astronomy, University of Missouri–St. Louis, 8001 Natural Bridge Road, St. Louis, Missouri 63121
Electronic mail: giblin@ssl.msfc.nasa.gov

JOHN T. RAYNER
Institute for Astronomy, 2680 Woodlawn Drive, Honolulu, Hawaii 96822
Electronic mail: rayner@galileo.ifa.hawaii.edu

HANS ZINNECKER
Astrophysikalisches Institut Potsdam, An der Sternwarte 16, D-14482 Potsdam, Germany
Electronic mail: hzinnecker@aip.de

Received 1997 February 20; revised 1997 August 5; accepted 1997 August 6

ABSTRACT

Infrared images of the R Coronae Australis molecular core in broad-band J, H, and K' filters and in narrow-band [Fe II] and H_2 filters are used to investigate star formation in this nearby cloud. Broad-band images with completeness limits of $J=17.5$, $H=17.0$, and $K'=16.5$ mag have revealed a total of 253, 482, and 692 sources, respectively. Color-color and color-magnitude diagrams are used to identify sources associated with the cloud and their evolutionary states. Assuming an age of 3×10^6 years, our H and K observations have completely sampled young stellar objects with $M>0.1$ $M_\odot$ through about 80% of the depth of the molecular core. As few as 22, and as many as 40, sources are associated with the cloud. In addition, there are five brown dwarf candidates. The large number of background stars in our sample is the key to the proper interpretation of our color-color diagram. As a result, only 8 sources are observed to have infrared excesses at K', implying a disk frequency for the association members between 16% and 35%. A focus of our study is the Coronet cluster, a compact group of ~10 young stellar objects associated with the star R Cr A. We find that these objects are associated with extensive reflection nebulae, dust-free cavities, and Herbig-Haro (HH) objects. Detailed study of the HH complexes 99A & B and 104C & D suggests they are associated with winds from cluster members IRS 9 and IRS 5 and/or IRS 6, respectively. The true position of the most deeply embedded cluster member, IRS 7, is established through 10 μm imaging. It appears that young stellar objects in this cluster have formed nearly simultaneously and undoubtedly influenced the formation and evolution of their nearest neighbors. © *1997 American Astronomical Society.* [S0004-6256(97)02711-8]

1. INTRODUCTION

Infrared arrays have dramatically changed our view of star formation by giving us the ability to observe low-mass young stellar objects (YSOs) in their natal molecular clouds. For example, observations of giant molecular clouds have revealed many examples of embedded clusters of high- and low-mass stars, ranging from the relatively nearby Trapezium and L 1630 clusters in Orion (McCaughrean & Stauffer 1994; Lada *et al.* 1991), to clusters associated with more distant OB stars and ultracompact H II regions (e.g., Hodapp & Rayner 1991; Rayner *et al.* 1991; Carpenter *et al.* 1993; Zinnecker *et al.* 1993).

[1]Current address: Department of Physics, University of Alabama at Huntsville, Huntsville, AL 35899.

 0004-6256/97/114(5)/2029/14/$10.00

It is in low-mass dark clouds within 200 pc of the Sun that infrared arrays can provide the most complete picture of low-mass star formation. First, infrared arrays are not only sensitive to the lowest mass objects in nearby clouds, but should sample brown dwarf stars through a significant fraction of the cloud depth. For example, YSOs of 0.1 $M_\odot$ are predicted to have a K (2.2 μm) magnitude of 11.6 at an age of 3 $\times 10^6$ years and a distance of 150 pc (D'Antona & Mazzitelli 1994). Thus, observations of a cloud at this distance to a limiting magnitude of $K=16.5$ mag should completely sample all YSOs of ≥ 0.1 $M_\odot$ through as much as 45 mag of visual extinction. Second, the high spatial resolution afforded by infrared imaging in nearby clouds can be used to study the binary frequency of YSOs and the structure of infrared reflection nebulae associated with YSOs on scales of a few hundred AU. Third, sites of active star formation often contain regions of extended infrared line emission both from gas radiatively excited by the ionizing flux of the most massive stars, and from the mechanically excited gas in shocks, as collimated jets and outflows from lower mass stars interact with the surrounding medium. Unlike the corresponding optical lines, this infrared emission is relatively unaffected by intracloud dust. Finally, deep infrared images may also be sensitive to large numbers of background stars shining through the cloud. This offers a tremendous advantage in the analysis of a region, supplying a comparison sample of field stars in the same direction as the cloud.

At a distance of 130 pc from the Sun (Marraco & Rydgren 1981), the Corona Australis molecular complex is one of the nearest star-forming regions. It is dominated by a centrally-condensed core centered near the emission line star R Cr A. The core, as defined by H_2CO and $C^{18}O$ observations, is $11' \times 20'$ in extent (0.4 pc $\times$ 0.7 pc) and contains about 50 $M_\odot$ of molecular gas (Harju *et al.* 1993; Loren *et al.* 1983). In addition to R Cr A (A5e), the most massive stars associated with this core are TY Cr A (B9), HD 176386 (A0), and T Cr A (F0e) (Herbig & Bell 1988). The highest density region of the R Cr A core is delineated by millimeter-wave continuum and CS(5–4) and (7–6) emission covering a $2'$ diameter region centered on the embedded source IRS 7 (also known as R1; Henning *et al.* 1994; Saraceno *et al.* 1996; Hezel *et al.* 1994). The total visual extinction through the densest part of the core is estimated from the $C^{18}O$ column density to be $A_v \sim 35$ mag (Wilking *et al.* 1992). Large scale Hα and infrared surveys have revealed that stars have formed throughout the Corona Australis cloud, with a concentration of YSOs in the R Cr A cloud core (Marraco & Rydgren 1981; Vrba *et al.* 1976; Wilking *et al.* 1992). A compact embedded cluster of ~ 10 objects, dubbed the Coronet, was found surrounding the star R Cr A in an infrared survey of the core ($K<14$ mag; Taylor & Storey 1984).

The sensitivity of near-infrared array cameras now makes it possible to survey the same cloud core a factor of ten times deeper than before, allowing us to probe for the lowest-mass stars through considerable extinction. In this paper, we describe the results of the first infrared imaging survey of the R Cr A cloud core: a preliminary analysis was previously reported by Wilking *et al.* (1994). In addition, we present narrow-band infrared images of shock-excited regions associated with Herbig-Haro objects 99 and 104. With these data, we discuss the membership of the association, the disk frequency, and star formation in the core center. The binary frequency in the association is discussed in Appendix B. We defer the subject of the mass function of the R Cr A cluster to a future paper which will include infrared spectroscopy of the brighter association members.

2. OBSERVATIONS AND ANALYSIS

2.1 Broad-Band Imaging with the IfA NICMOS3 Camera

A 170 square arcminute region of the Cr A cloud was imaged at J (1.25 μm), H (1.65 μm), and K' (2.11 μm). The region extends from TY Cr A and HD 176386 in the northwest, through the dense cloud core and the star R Cr A, and along the molecular cloud ridge to the southeast. Figure 1 shows the full J-band survey mosaic, with $C^{18}O$ contours from Harju *et al.* (1993) superimposed. Our mosaic covers 82% of the high column density gas in the Cr A cloud observed in the Harju *et al.* survey, i.e., areas of the cloud where the $C^{18}O$ integrated intensity is greater than 2 K km sec^{-1} which implies A_v exceeds ~ 15 mag.[2] The infrared observations were made using the Institute for Astronomy 256$\times$256 pixel NICMOS3 camera (Hodapp *et al.* 1992) on the University of Hawaii 88-inch telescope in 1991 July. The K' filter was used for its lower thermal background relative to the standard K passband (Wainscoat & Cowie 1992). The image scale of the array was 0.75″ $pixel^{-1}$, giving a field-of-view of $3.2' \times 3.2'$. Twenty-nine spatial positions were observed, accompanied by a dithered observation offset by 10″. Integration times at J, H, and K' for each pointing of telescope were 60, 30, and 30 seconds. An overlapping mapping scheme was employed such that the central two-thirds of the region was covered by four independent observations and the outer third by two. Briefly, the data were reduced first by subtracting a clean stack of sky images taken $\sim 30'$ north of R Cr A, then dividing by a flat field formed by using the difference between images of the inside of the dome with and without tungsten illumination.

2.2 Narrow-band Imaging with IRIS

Narrow-band images were obtained of two regions centered on Herbig-Haro objects HH 99A & B (Cohen *et al.* 1984) and HH 104C & D (Graham 1993). The observations were made using the IRIS 128$\times$128 NICMOS2 camera (Allen *et al.* 1993) on the 3.9-m Anglo-Australian Telescope in 1994 July. Filters of 1% spectral resolution centered on the lines of H_2 $v=1-0$ $S(1)$ (2.12 μm), Br γ (2.16 μm), and [Fe II] (1.64 μm), and at 4% resolution on the continuum (2.21 μm) were used. The image scale of 0.61″ $pixel^{-1}$ gave a $1.3' \times 1.3'$ field-of-view. In each filter, the source was observed in a 3$\times$3 grid with 30″ offsets between frames. Inte-

[2]This correspondence between A_v and $C^{18}O$ integrated intensity assumes $T_{ex}=25$ K, LTE conditions, and the relationship between A_v and $C^{18}O$ column density derived for the ρ Oph cloud by Wilking & Lada (1983). The uncertainty in the visual extinction derived in this manner is estimated to be 30%–50%.

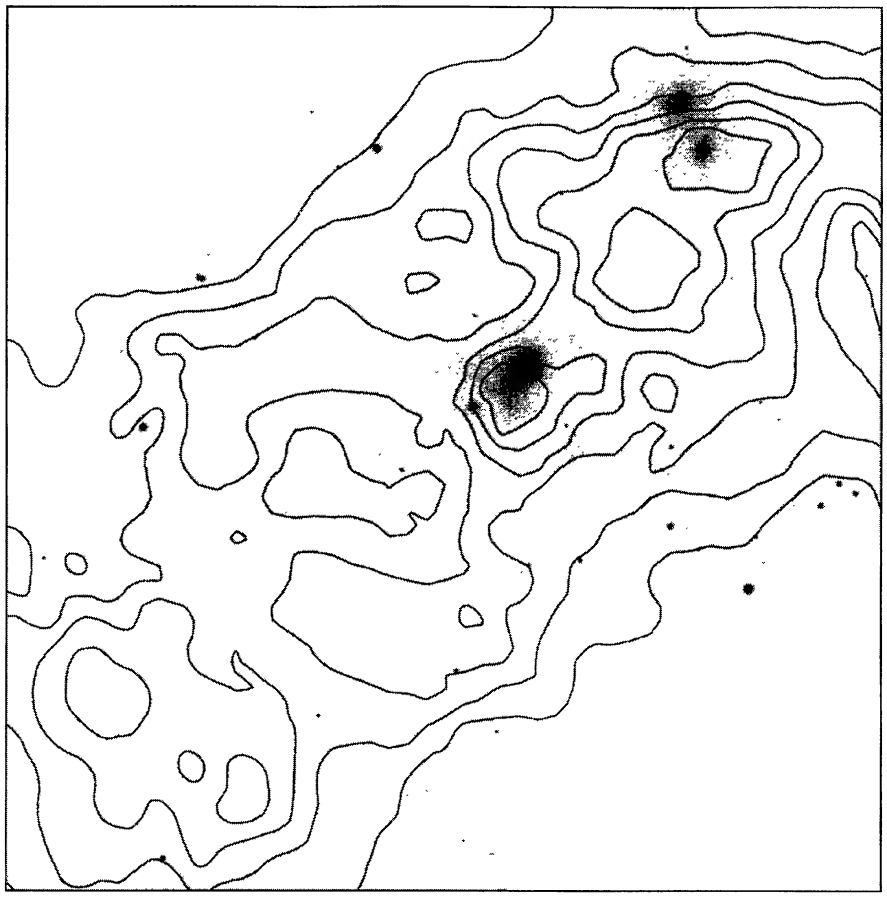

FIG. 1. The full 15×15 arcmin J-band mosaic with contours of $C^{18}O$ (1→0) integrated intensity superposed. The $C^{18}O$ (1→0) contours are from the 45 arcsec resolution SEST observations by Harju *et al.* (1993). The outer contour is 1.0 K km s^{-1} and increases in intervals of 0.5 K km s^{-1} to a maximum of 3.5 K km s^{-1}. Our infrared survey encompasses 82% of the high column density gas in the Harju *et al.* observations with integrated intensities >2 K km s^{-1}. This roughly corresponds to areas of the cloud where A_v is greater than 15 mag.

gration times were 1 minute per frame. The data were sky subtracted using the median of all frames in a given filter, and then flat-fielded using halogen lamp dome flats.

2.3 Photometry in the Broad-Band Survey

Source identification and photometry were performed using the DAOPHOT and APPHOT packages in IRAF. A total of 692 unsaturated sources were identified in the K' mosaic at a peak intensity level of at least five times the RMS background noise. Of this sample, a total of 482 sources were also detected at H, and 253 at J. The number of sources seen at shorter wavelengths decreases due to the higher opacity of the cloud to background stars and stronger scattered nebular emission from early-type stars in the cloud. All photometry was obtained using an aperture of 3.5″ in diameter; at roughly twice the stellar FWHM, this resulted in optimal signal-to-noise (Howell 1989). Corrections for the wings of the source profile at each wavelength were determined by constructing an aperture curve-of-growth for bright, unsaturated stars in the mosaic. A sky annulus that extended from 3″ to 10.5″ from the source center was used to subtract the background sky from the aperture. The photometry was calibrated using observations of the standard star HD 225023 (Elias *et al.* 1982). Atmospheric extinction corrections of 0.12, 0.06, and 0.10 mag airmass^{-1} were determined at J, H, and K', respectively.

The survey is incomplete at the bright end due to detector saturation at fluxes corresponding to 11.5, 11.0, 10.5 mag at J, H, and K', respectively. At the faint end, completeness limits were estimated by adding and attempting to recover ~100 artificial stars in each mosaic. The 90% completeness limits were reached at 17.5, 17.0, and 16.5 mag at J, H, and K'.

The photometry is presented in Table 1 in the natural photometric system of the instrument for 125 sources with $K'<15$ mag, plus a star-like object associated with nebulosity with $K'=15.73$. A complete table of photometry and astrometry for the full source list down to $K'=16.5$ mag is available on request. The statistical errors given in Table 1 were calculated from the sum of the squares of errors from poisson sky noise in the aperture, poisson noise from the star, and the error in the mean sky. In most cases the statistical errors are less than the uncertainty in the photometric calibration. This is estimated to be about 0.04 mag and is

TABLE 1. Infrared photometry from NICMOS3 array.

RA(1950)	DEC(1950)	J	σ_J	H	σ_H	K'	$\sigma_{K'}$	Name[a]
$18^h58^m01\overset{s}{.}0$	−37°01′02″	···	···	13.14	0.00	12.74	0.00	
18 58 02.5	−36 59 56	14.81	0.01	13.66	0.01	13.22	0.01	
18 58 02.8	−36 59 27	16.46	0.02	15.22	0.02	14.66	0.02	
18 58 03.7	−36 58 21	17.42	0.04	15.71	0.03	14.84	0.02	
18 58 05.3	−36 56 35	16.76	0.03	15.23	0.02	14.60	0.02	
18 58 08.4	−37 03 53	15.86	0.01	14.53	0.01	14.23	0.01	
18 58 08.4	−36 57 49	···	···	16.62	0.07	14.78	0.02	
18 58 08.9	−37 02 01	16.91	0.03	15.46	0.03	14.78	0.02	
18 58 09.2	−37 04 50	···	···	13.71	0.01	13.29	0.01	
18 58 09.5	−37 02 49	17.87	0.08	16.01	0.04	14.76	0.02	
18 58 09.7	−37 01 59	17.22	0.04	15.79	0.03	14.90	0.02	
18 58 09.8	−37 02 24	14.57	0.00	12.54	0.00	11.53	0.00	IRS 14 (TS 2.9)
18 58 10.7	−37 02 40	17.22	0.04	15.27	0.02	14.23	0.01	
18 58 11.0	−37 04 52	15.37	0.01	14.61	0.02	14.28	0.02	
18 58 11.4	−37 02 06	14.07	0.00	11.74	0.00	10.55	0.00	IRS 13 (TS 2.8)
18 58 11.7	−37 04 25	12.85	0.00	12.15	0.00	11.75	0.00	
18 58 13.3	−36 55 29	15.56	0.01	14.18	0.01	13.66	0.01	
18 58 13.3	−36 56 57	18.39	0.18	16.00	0.05	14.77	0.02	
18 58 13.8	−37 02 25	···	···	16.35	0.06	14.94	0.02	
18 58 14.1	−37 00 00	14.81	0.01	14.24	0.01	13.88	0.01	
18 58 14.9	−37 04 58	16.64	0.04	15.57	0.04	14.90	0.04	
18 58 15.3	−37 04 35	14.35	0.00	13.19	0.01	12.43	0.00	K excess[b]
18 58 15.4	−37 03 50	15.68	0.01	13.83	0.01	13.08	0.00	
18 58 16.6	−37 04 39	14.33	0.01	13.03	0.01	12.41	0.00	
18 58 17.3	−36 55 21	16.07	0.02	14.11	0.01	13.59	0.01	
18 58 17.8	−37 02 33	···	···	17.18	0.16	14.08	0.01	
18 58 17.9	−36 56 47	···	···	14.65	0.03	13.99	0.02	
18 58 18.2	−36 56 03	13.68	0.00	11.56	0.00	10.63	0.00	
18 58 19.4	−37 01 20	17.67	0.07	14.80	0.02	13.34	0.01	IRS 11 (TS 2.5)
18 58 19.6	−36 56 50	···	···	15.52	0.06	14.93	0.05	
18 58 22.4	−36 56 07	17.82	0.09	15.78	0.03	14.92	0.03	
18 58 23.2	−36 58 05	···	···	15.97	0.04	14.47	0.01	
18 58 24.1	−37 05 11	16.31	0.03	15.03	0.02	14.56	0.02	
18 58 25.4	−37 03 52	16.75	0.03	13.86	0.01	12.42	0.00	IRS 15 (TS 13.4)
18 58 25.6	−37 01 44	···	···	13.73	0.01	10.59	0.00	IRS 5 (TS 2.4,neb)
18 58 26.8	−37 04 50	12.54	0.00	11.81	0.00	11.64	0.00	
18 58 27.5	−36 55 50	15.84	0.01	14.63	0.01	14.10	0.01	
18 58 28.0	−37 01 00	···	···	12.87	0.01	10.74	0.00	IRS 6 (TS 2.3,neb)
18 58 28.5	−37 02 40	···	···	16.52	0.09	14.52	0.06	
18 58 28.8	−36 58 34	14.73	0.00	12.63	0.00	11.52	0.00	IRS 8 (TS 2.2)
18 58 30.2	−37 01 22	···	···	13.37	0.01	11.67	0.01	IRS 9 (R2)
18 58 30.7	−36 55 42	16.86	0.03	15.01	0.02	14.30	0.02	
18 58 30.8	−37 05 36	17.99	0.11	15.72	0.04	14.65	0.02	
18 58 30.9	−37 09 22	···	···	14.97	0.02	14.61	0.02	
18 58 31.1	−37 04 56	14.06	0.00	13.44	0.00	13.09	0.01	Star A[c]
18 58 32.4	−37 00 50	···	···	15.59	0.07	14.44	0.05	
18 58 32.8	−37 01 44	···	···	13.49	0.11	12.22	0.07	IRS 7 (R1,neb)
18 58 33.9	−37 07 47	14.49	0.00	13.35	0.00	12.91	0.00	
18 58 34.0	−37 00 58	···	···	15.75	0.09	14.15	0.05	
18 58 34.2	−37 09 53	14.81	0.01	13.79	0.01	13.33	0.01	
18 58 34.6	−37 01 22	···	···	16.36	0.14	14.64	0.04	
18 58 34.7	−37 07 35	15.63	0.01	14.04	0.01	13.36	0.01	
18 58 35.5	−37 09 25	16.24	0.02	15.24	0.02	14.78	0.02	
18 58 35.7	−37 04 50	18.33	0.11	15.22	0.02	13.75	0.01	
18 58 36.1	−37 01 31	···	···	15.53	0.12	13.97	0.06	
18 58 36.2	−37 00 40	13.82	0.00	11.28	0.00	sat.	···	IRS 4 (TS 4.1)
18 58 36.3	−37 04 04	16.95	0.04	14.32	0.01	13.00	0.00	
18 58 36.4	−36 57 58	15.97	0.02	13.63	0.01	12.56	0.00	
18 58 36.5	−37 04 28	18.25	0.10	15.74	0.02	14.51	0.02	
18 58 36.7	−37 09 40	15.18	0.01	14.17	0.01	13.76	0.01	
18 58 36.7	−37 08 32	15.77	0.01	14.95	0.02	14.70	0.02	
18 58 37.2	−36 58 32	17.90	0.08	15.77	0.04	14.77	0.02	
18 58 37.5	−37 06 45	11.88	0.00	11.29	0.00	11.12	0.00	
18 58 38.4	−37 03 12	16.06	0.02	14.36	0.01	13.55	0.01	
18 58 38.9	−37 03 14	17.74	0.09	15.70	0.03	14.85	0.03	
18 58 38.9	−37 09 32	16.47	0.03	15.29	0.02	14.90	0.02	
18 58 39.5	−37 10 04	15.84	0.01	14.78	0.01	14.52	0.02	

TABLE 1. (continued)

RA(1950)	DEC(1950)	J	σ_J	H	σ_H	K'	$\sigma_{K'}$	Name[a]
18 58 39.6	−36 58 23	···	···	17.02	0.11	15.73	0.06	neb[d]
18 58 39.9	−37 08 49	15.30	0.01	14.23	0.01	13.83	0.01	
18 58 40.4	−37 04 33	···	···	16.45	0.06	14.82	0.02	neb[d]
18 58 40.7	−37 10 34	14.11	0.00	13.44	0.01	13.21	0.01	
18 58 41.6	−37 08 54	15.16	0.01	14.18	0.01	13.84	0.01	
18 58 41.6	−37 01 24	···	···	15.11	0.02	13.28	0.01	IRS 10 (TS 4.2)
18 58 43.9	−36 59 44	···	···	16.22	0.05	14.89	0.02	
18 58 43.9	−37 06 07	···	···	16.15	0.03	14.86	0.02	
18 58 44.2	−36 58 36	15.98	0.02	14.72	0.01	14.17	0.01	
18 58 44.2	−37 03 04	15.63	0.01	14.59	0.01	14.00	0.01	
18 58 45.5	−36 58 17	15.97	0.02	14.31	0.01	13.49	0.01	
18 58 47.7	−37 01 11	···	···	16.60	0.06	14.05	0.01	
18 58 48.1	−36 58 08	13.92	0.00	12.61	0.00	11.96	0.00	
18 58 48.2	−37 08 18	17.32	0.03	15.61	0.02	14.90	0.02	
18 58 48.8	−37 07 30	16.02	0.01	14.28	0.01	13.47	0.01	
18 58 49.3	−37 07 33	13.46	0.00	12.59	0.00	12.45	0.00	
18 58 50.4	−36 57 12	14.53	0.01	13.64	0.01	13.25	0.01	
18 58 50.5	−37 06 23	17.46	0.04	15.00	0.01	13.87	0.01	
18 58 50.6	−37 06 18	···	···	15.71	0.03	13.95	0.01	
18 58 51.1	−37 00 02	18.03	0.08	15.78	0.03	14.59	0.01	
18 58 51.6	−37 03 55	16.89	0.03	15.50	0.02	14.89	0.02	
18 58 52.0	−37 04 56	···	···	15.39	0.02	13.20	0.01	
18 58 52.0	−37 06 32	18.55	0.09	16.07	0.04	14.76	0.02	
18 58 52.2	−37 04 05	15.84	0.01	14.18	0.01	13.53	0.01	
18 58 53.3	−37 03 28	16.54	0.02	14.84	0.01	13.81	0.01	K excess[b]
18 58 56.5	−37 10 21	16.06	0.02	14.72	0.01	14.23	0.01	
18 58 56.9	−37 08 34	18.45	0.10	14.62	0.01	12.61	0.00	
18 58 58.1	−36 59 27	16.42	0.02	15.25	0.02	14.86	0.02	
18 58 58.7	−37 03 59	17.16	0.03	14.10	0.01	12.59	0.00	
18 58 59.0	−36 59 39	15.57	0.01	14.48	0.01	14.15	0.01	
18 58 59.4	−37 06 48	···	···	16.57	0.06	14.87	0.02	
18 58 59.9	−37 00 02	12.44	0.00	11.54	0.00	11.24	0.00	GP wb
18 59 00.2	−37 04 35	17.97	0.06	15.73	0.02	14.99	0.02	
18 59 00.7	−37 10 19	15.84	0.02	14.68	0.01	13.83	0.01	
18 59 00.8	−37 04 58	18.06	0.08	15.87	0.03	14.88	0.02	
18 59 01.7	−37 07 10	18.09	0.07	15.37	0.02	13.91	0.01	
18 59 02.0	−37 10 32	16.01	0.02	14.53	0.01	13.97	0.01	
18 59 02.4	−37 05 24	16.87	0.02	15.09	0.01	14.24	0.01	
18 59 03.0	−37 04 20	16.88	0.03	14.67	0.01	13.60	0.01	
18 59 03.5	−37 09 39	17.80	0.06	15.65	0.03	14.93	0.03	
18 59 04.3	−37 00 25	16.81	0.03	15.35	0.02	14.74	0.02	
18 59 04.7	−37 04 26	16.29	0.02	14.44	0.01	13.69	0.01	
18 59 05.7	−37 00 47	16.35	0.02	14.07	0.01	12.99	0.01	
18 59 06.4	−37 07 54	14.69	0.00	11.92	0.00	10.84	0.00	
18 59 06.5	−37 01 20	15.15	0.01	13.29	0.00	12.46	0.00	
18 59 07.0	−37 00 33	16.98	0.04	15.28	0.02	14.44	0.02	
18 59 07.2	−37 10 06	16.02	0.01	14.78	0.01	14.24	0.01	
18 59 07.9	−37 03 25	16.47	0.03	15.02	0.02	14.49	0.02	
18 59 08.2	−37 05 09	16.29	0.01	14.96	0.01	14.49	0.01	
18 59 09.7	−37 10 11	16.12	0.02	15.13	0.02	14.81	0.02	
18 59 09.7	−37 07 08	···	···	15.78	0.04	14.19	0.01	
18 59 11.4	−37 05 12	16.98	0.03	15.64	0.03	14.97	0.03	
18 59 11.8	−37 09 13	17.04	0.04	15.48	0.03	14.82	0.03	
18 59 12.9	−37 04 53	13.91	0.00	12.98	0.00	12.58	0.00	
18 59 14.1	−37 07 25	16.04	0.01	13.96	0.01	13.10	0.01	
18 59 14.4	−37 08 54	16.84	0.03	15.31	0.02	14.69	0.02	
18 59 15.2	−37 06 04	16.55	0.03	14.87	0.02	14.18	0.01	
18 59 15.6	−37 10 11	16.59	0.03	14.87	0.02	14.18	0.01	
18 59 15.6	−37 09 50	16.17	0.02	14.47	0.01	13.74	0.01	

[a]Sources previously identified by Taylor & Storey (IRS/TS 1984), Glass & Penston (GP, 1975), or Graham (1993). "neb" indicates association with near-infrared nebulosity.
[b]Newly identified infrared excess source from Fig. 6(b).
[c]Star with strong Hα emission identified by Graham (1993).
[d]New association member identified through nebulous appearance.

TABLE 2. Infrared photometry of bright sources.

RA(1950)	DEC(1950)	J	H	K	L	Ref.[a]	Source Name[b]
$18^h58^m00^s.6$	−37°00′56″	11.18	9.71	9.12	···	ESO(1)	
		0.03	0.02	0.03	···		
18 58 02.9	−37 03 44	11.74	9.81	8.65	7.25	ESO(1)	VSS 18
		0.05	0.02	0.01	0.06		
18 58 04.4	−37 03 33	10.84	10.17	10.13	···	ESO(1)	GP e2
		0.03	0.03	0.07	···		
18 58 05.9	−37 03 56	10.96	9.68	9.06	8.47	ESO(1)	x-ray[c]
		0.04	0.02	0.02	0.35		
18 58 12.2	−37 05 23	8.81	8.07	7.82	7.57	ESO(1)	Anon1/VSS 13/CrA x1
		0.01	0.01	0.01	0.09		
18 58 16.6	−36 57 44	6.95	6.85	6.78	···	AAO(2)	HD 176386a (neb)
18 58 16.8	−36 57 47	···	9.10	8.88	···	IRTF(3)	HD 176386b (neb)
18 58 17.8	−36 55 57	14.13	11.73	10.50	8.99	ESO(1)	
		0.17	0.03	0.03	0.29		
18 58 18.6	−36 56 50	7.55	6.99	6.70	···	AAO(4)	TY Cr A (neb)
18 58 19.1	−37 02 48	13.96	9.89	7.16	···	AAO(2)	IRS 2 (TS 13.1,neb)
18 58 19.1	−37 04 18	10.55	9.11	8.39	7.36	ESO(1)	Hα 2/Star 1-100
		0.02	0.02	0.02	0.10		
18 58 25.6	−37 01 39	17.54	13.65	10.33	···	AAO(2)	IRS 5 (TS 2.4,neb)
18 58 28.2	−37 00 58	16.35	12.71	10.34	···	AAO(2)	IRS 6 (TS 2.3,neb)
18 58 28.3	−37 02 30	16.41	11.54	8.04	···	AAO(2)	HH 100-IR (TS 2.6,neb)
18 58 30.7	−37 01 24	17.77	14.66	11.97	···	AAO(2)	IRS 9 (R2)
18 58 31.7	−37 01 30	8.55	6.01	4.13	···	AAO(2)	R Cr A (neb)
18 58 36.5	−37 00 39	14.04	11.28	9.87	···	AAO(2)	IRS 4 (TS 4.1)
18 58 36.5	−37 02 10	10.81	9.93	8.20	···	AAO(2)	T Cr A (neb)
18 58 41.9	−37 01 23	18.43	15.08	13.13	···	AAO(2)	IRS 10 (TS 4.2)
18 58 42.7	−37 03 17	12.92	10.66	8.64	···	AAO(2)	IRS 3 (TS 4.4)
18 58 44.9	−36 57 48	9.39	7.47	6.49	5.74	ESO(1)	VSS 7
		0.01	0.01	0.01	0.03		
18 59 00.4	−36 59 59	10.29	9.38	9.07	···	ESO(1)	GP wa/CrA x3
		0.02	0.02	0.01	···		
18 59 03.8	−37 10 05	11.59	9.92	9.21	8.50	ESO(1)	
		0.05	0.03	0.02	0.30		
18 59 04.3	−37 02 38	9.17	8.14	7.82	···	SAAO(5)	Hα 14

[a]Origin of photometric data: ESO(1), this study; AAO(2), Taylor & Storey (1984); IRTF(3), Wilking *et al.* (1992); AAO(4), Taylor & Storey (unpublished data); SAAO(5), Glass & Penston (1975).
[b]Source names taken from Vrba *et al.*(VSS, 1976), Glass & Penston (GP, 1975), Walter (CrAx, 1986), Taylor & Storey (IRS/TS, 1984), Knacke *et al.* (Anon1, 1973), Marraco & Rydgren (Hα, 1981), and Graham (Star1-100, 1993). "neb" indicates the presence of near-infrared nebulosity.
[c]*ROSAT* x-ray source (Patten 1994).

dominated by variations in the flatness of the array (~2%) and uncertainties in corrections for atmospheric extinction (~3%). Source positions were determined relative to a reference frame established by the positions of 13 astrometric standards in our mosaic kindly provided by Burt Jones. Positions calculated in this frame are accurate to ±1″.

Table 2 presents supplemental photometry for 24 sources that were either too bright or too faint to be measured at one or more wavelengths in the imaging survey. Aperture photometry at J, H, K (2.2 μm), and L (3.5 μm) was acquired using the ESO infrared photometer on the La Silla 1-m telescope in 1993 July. An aperture of 15″ in diameter and chopper throws of 20–30″ were used. Aperture photometry at J, H, and K for another 12 sources was taken from Taylor & Storey (1984 and unpublished data). Their data were obtained on the 3.9-m Anglo-Australian telescope using a 5″ diameter aperture for all but R Cr A and IRS 5, where a 3.5″ aperture was used. Aperture photometry for the emission-line star Hα 14 (KS 15) was taken from Glass & Penston (1975) who used a 12″ aperture. Finally, H and K photometry for the companion to HD 176386 were taken from Wilking *et al.* (1992), who used ProtoCAM on the IRTF. All these photometry measurements are presented in their respective natural photometric systems in Table 2.

To allow the construction of uniform color-color and color-magnitude diagrams, all photometry was transformed into the system described by Bessell & Brett (1988). Data for a given source were adopted wholesale from either Table 1 or Table 2, i.e., from a coherent set of JHK photometry, with preference always given to the survey data in Table 1. Appendix A describes in detail how these transformations were made.

3. RESULTS

3.1 Three-Color Image

Shown in Fig. 2 (Plate 97) is the central region of the infrared mosaic of the R Cr A infrared cluster at J (blue), H (green), and K' (red). The area shown is 8.6′×9.1′. K' images of the region with labels for the bright stars, infrared sources, x-ray sources, Herbig-Haro objects, and nebulous

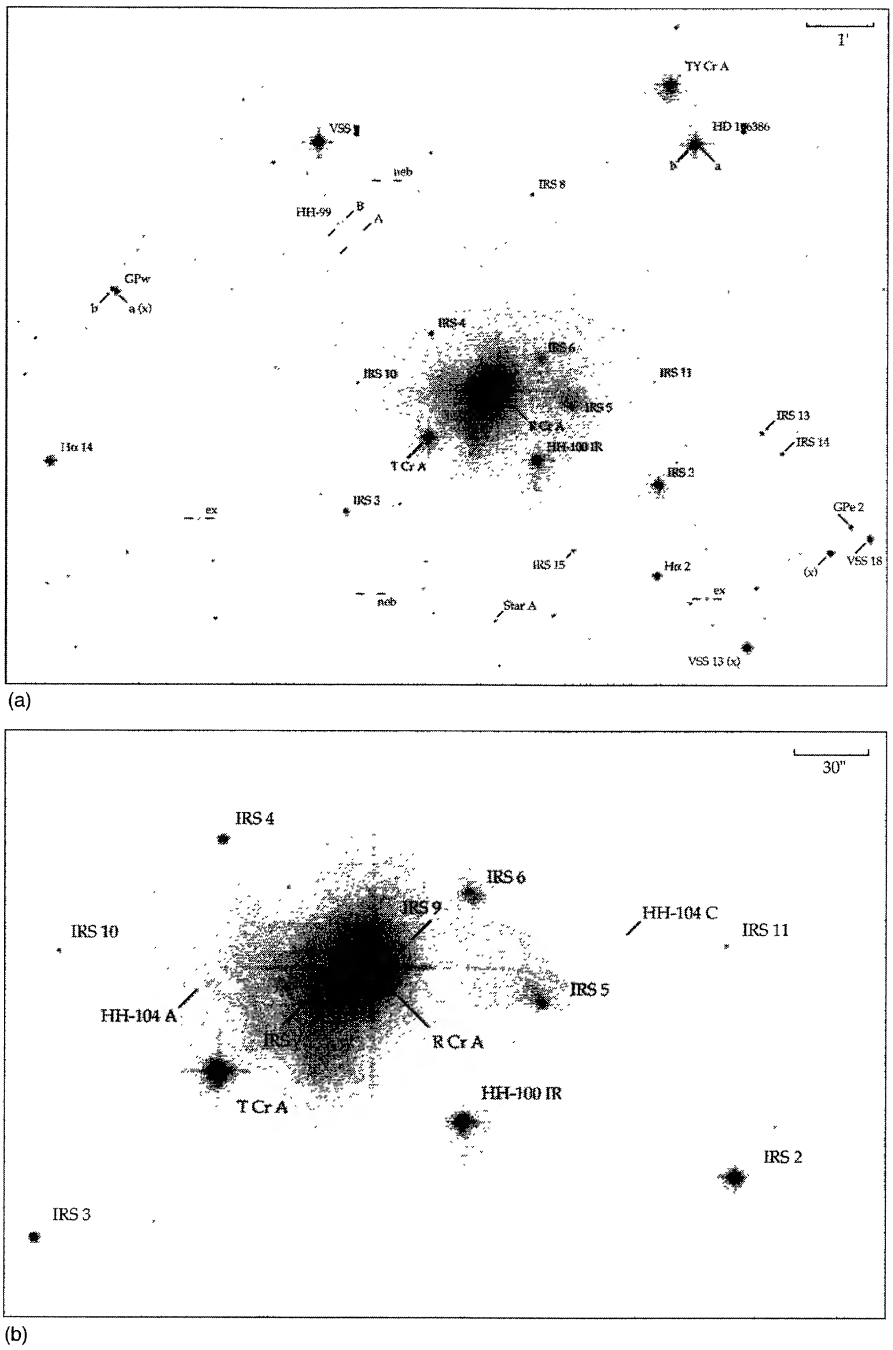

FIG. 3. Source identifications on the K' mosaic of the R Cr A cloud core. In (a), a broad perspective is shown covering an area 13.5×10 arcmin. Labeled in the diagram are prominent stars, infrared sources, nebulous objects (neb), x-ray sources (x), and HH objects. IRS 3 and the two stars labeled as "ex" are newly identified objects with infrared excesses. (b) shows an expanded view of the R Cr A region, identifying the nebulous object IRS 7 and the star IRS 9 which lie close to the star R Cr A as well as HH objects 104A&C.

objects are presented in Figs. 3(a) and 3(b). IRS 3 and the two stars labeled as "ex" are newly identified objects with infrared excesses. In addition to the star R Cr A and its associated nebulosity are the early type stars TY Cr A and HD 176386 and their bluish reflection nebulae (northwest) and the emission-line star T Cr A (southeast). All of the brighter members of the Coronet infrared cluster are associated with infrared reflection nebulae: starting north of R Cr A and moving clockwise are IRS 6, IRS 5, IRS 2, HH 100-IR and T Cr A. IRS 2 and HH 100-IR lie adjacent to bubble-like cavities about 1′ in diameter most likely swept clean of dust by their stellar winds. These features suggest a common age for YSOs in the Coronet. Herbig-Haro objects 99A and B lie to the northeast of R Cr A. HH 99B displays a bullet-like morphology at J and H ([Fe II] emission) trailed by a bow shock and wake seen at K' (shocked molecular hydrogen).

3.2 Notes on Individual Sources

3.2.1 IRS 7

Raster scan maps at 2 μm by Taylor & Storey (1984) revealed this nebulous object 19″ east and 15″ south of the star R Cr A. They also refer to this object as R1. Subsequent studies at millimeter wavelengths found that IRS 7 is an extremely young object associated with strong, compact emission from cold dust, CS, and $C^{18}O$ (Harju *et al.* 1993; Henning *et al.* 1994; Saraceno *et al.* 1996; Hezel *et al.* 1994). VLA observations at $\lambda = 6$ cm indicated that IRS 7 lies between two radio sources separated by 14″ (Brown 1987). It was proposed that the radio emission is excited by a bipolar outflow from the YSO. In our images, IRS 7 is not revealed as a point source and is confused with a ridge of nebulosity immediately to the east and north [Fig. 3(b)]. In 1994 May, we obtained an image of the region at $\lambda = 10$ μm using the TIMMI camera at the ESO 3.6-m telescope using 0.56″ pixel^{-1}. The image does show a distinct point source in the vicinity of IRS 7, but only 17.5″ east and 12.3″ south of the star R Cr A, i.e., a 3.1″ offset from the near-infrared source. Therefore, we are probably not observing the YSO directly at 2 μm, but rather a scattering surface offset some 500 AU from it. This new position for IRS 7 rules out the bipolar wind interpretation for the radio emission. The true position of the YSO lies within 1″ of the western radio source, IRS 7A. The eastern radio source coincides with no known near-infrared source and further study is needed to determine its nature.

3.2.2 HH 99A & B

HH 99A and HH 99B were first identified as a pair of compact knots in deep Hα photographs by Cohen *et al.* (1984). Subsequent raster scan maps in the $v = 1$–0 S(1) line of molecular hydrogen at 2.122 μm showed an extended region of shocked gas (Wilking *et al.* 1990).

Our higher resolution images [Figs. 2 and 4(a) and 4(b)] show that HH 99B is a bright knot of [Fe II] emission on the northeastern edge of the system trailed by a bright arc of H_2 emission 2.2″ to the southwest. The brightest H_2 emission is observed at the ends of the arc. As evident in color composite image in Fig. 2, the [Fe II] emission is the highest excitation section of a bow shock delineated by the H_2 emission. Fainter [Fe II] emission to the southwest forms a linear feature which points back to the Coronet cluster and appears to define the axis of an ionized jet. Surrounding the jet is extended and clumpy H_2 emission which appears as a wake of shocked molecular gas. This structure is reminiscent of HHs discovered in the IRc2 region of Orion (Allen & Burton 1993), believed to result from the ejection, then deceleration, of a dense clump of material from the core of the star-forming cloud. To the south-southwest of HH 99B lies HH 99A. Again, the [Fe II] and H_2 emission are offset (see Fig. 2), but in the opposite sense from HH 99B. The highest excitation gas appears to lie in the direction of the exciting star. Such a structure would suggest that HH 99A is a dense ambient clump or entrained material that is being shocked by the HH 99B jet.

It is interesting to note that previous studies have used the axis defined by HH 99A and HH 99B to identify HH 100-IR as the exciting star. However, in our images, the bow shock/jet define a position angle which is consistent with an origin from the infrared source IRS 9 or perhaps the star R Cr A. Alignment is most consistent with the IRS 9 and it seems the most likely candidate since the molecular outflow axis for R Cr A is oriented east-west (Levreault 1988, Graham 1993). We note that there is a faint continuum source visible at 2 μm ($K' = 15.63$) which lies on the axis defined by the linear [Fe II] emission and the H_2 emission. However unlike typical HH exciting stars, the colors for this source indicate no infrared excess, $(J-H) = 1.71 \pm 0.21$ and $(H-K) = 1.37 \pm 0.12$, and we suspect it is a field star.

A faint arc of emission, labeled "C" in Figs. 4(a) and 4(b), is seen in H_2 and, at its head, in [Fe II] to the east of HH 99A/B. It may trace the wind from another infrared source in the Coronet, or be the fossil cavity of a previous episode of ejection or mass loss from the same source that created HH 99A/B. This could occur, for instance, by precession of a jet, the proper motion of the driving source, or perhaps, as in the case of Orion, simply the ejection of another projectile prior to HH 99B but in a slightly different direction (Allen & Burton 1993).

3.2.3 HH 104C & D

Graham (1993) identified two faint [S II] emission knots to the west of the star R Cr A. He proposed that these objects, HH 104C and HH 104D, lie in the receding CO outflow from R Cr A and that, along with HH 104A and HH 104B to the east of the star, define the axis of the bipolar outflow from R Cr A. HH 104C is clearly present in our H and K' broad-band images [Fig. 3(b)]. Figures 4(c) and 4(d) shows the narrow-band [Fe II] and H_2 images of the region obtained with IRIS. A diffraction spike from the star R Cr A belies its present just off the eastern edge of the field. The bright infrared sources, IRS 5 and IRS 6, are associated with extensive reflection nebulosity and that surrounding IRS 5 has been the subject of intensive study (Castelaz & Hackwell 1987; Chen & Graham 1993). Emission from both [Fe II] and H_2 are observed from HH 104C and HH 104D, with HH 104C being significantly brighter in H_2. Fainter emission knots are apparent in the H_2 image only along a line between HH 104D and IRS 6 and delineate lower excitation knots.

Our images cast doubt as to the proposed association of HH 104C & HH 104D with HH 104A & B and the star R Cr A. The alignment of the H_2 knots in Fig. 4(d) points to IRS 6 as the possible exciting star for the entire system, with HH 104C and D representing the highest excitation gas. Alternatively, HH 104C and HH 104D are roughly aligned with IRS 5. Dynamical information will be necessary to understand completely this region.

3.3 Color-Magnitude and Color-Color Diagrams

Color-magnitude and color-color diagrams are useful tools to explore the nature of the sources observed in our deep NICMOS survey. For inclusion in this analysis, we required uncertainties in the $(J-H)$ and $(H-K)$ colors less

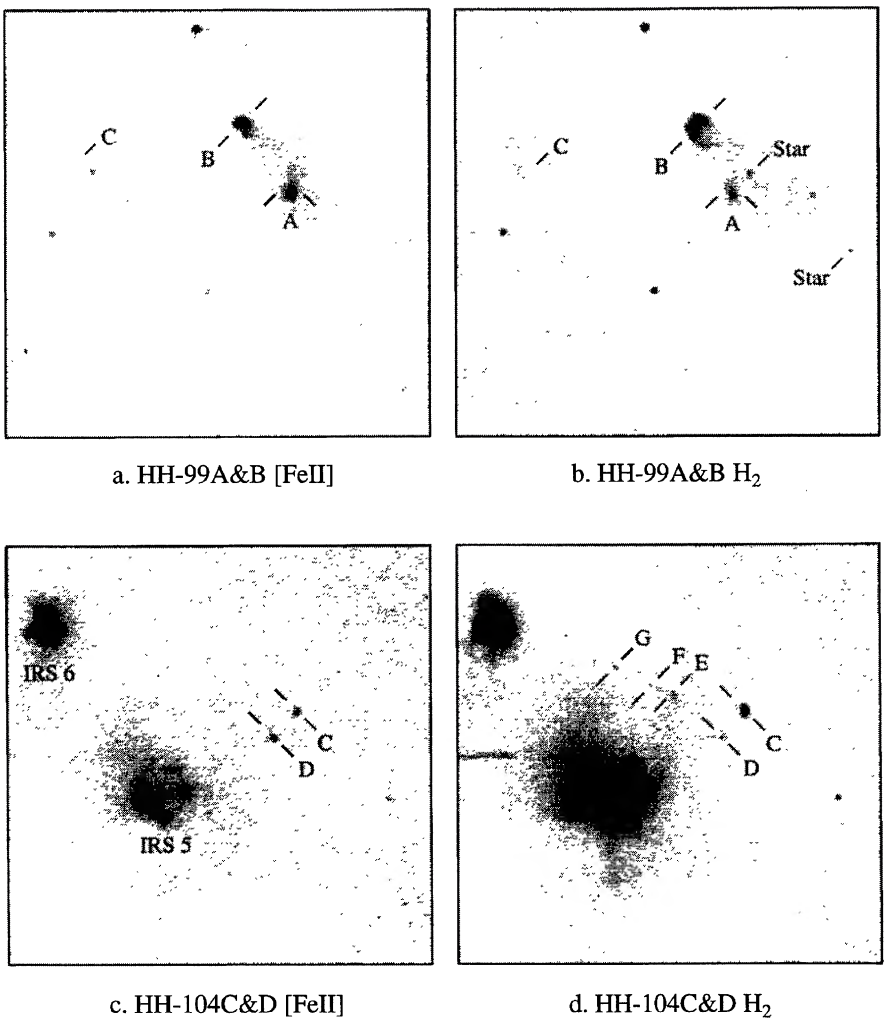

FIG. 4. Narrow-band images of the HH 99 and HH 104 regions. (a) and (b) present the individual [Fe II] and H_2 images shown in the color composite image in Fig. 2. In addition to HH 99A&B, a third feature (labeled "C") appears east of A. "C" has a filamentary structure nearly parallel to the extended emission trailing HH 99B, plus a faint knot of [Fe II] emission below the line pointing to "C." A faint wisp of H_2 emission below the label "B" may also be part of feature "C." (c) and (d) show the [Fe II] and H_2 emission from the HH 104 region. In addition to knots C & D, we identify new features in the H_2 image as "E," "F," & "G."

than or equal to 0.15 mag. There are 365 sources with $(H-K)$ colors and 235 sources with $(J-H)$ and $(H-K)$ colors which meet this criterion.

3.3.1 The slope of the reddening line

The number of sources with a K excess in a $(J-H)$ vs $(H-K)$ diagram is very sensitive to the slope of the reddening law for the cloud. This slope is known to vary from cloud to cloud and is a function of the average grain size (e.g., Steenman & Thé 1989). In our analysis, we have taken advantage of the large number of field stars in our sample and treated the slope as a free parameter. Therefore, we first identified a subset of our sources as diskless objects and used them to calibrate the value of $(J-H)/(H-K)$.

The K vs $(H-K)$ color-magnitude diagram in Fig. 5 was used to define the sample of diskless stars. For reference, we have shown the unreddened zero-age main sequence (ZAMS, shifted by 0.1 mag to the left for display purposes), and isochrones for 3×10^6 and 10^7 years assuming a distance of 130 pc. The isochrones were derived from the models of D'Antona & Mazzitelli (1994) using Alexander opacities and Canuto-Mazzitelli convection. Extensions of their models to include absolute infrared magnitudes as a function of mass and age were obtained using published intrinsic colors and bolometric corrections for dwarf stars (Schmidt-Kaler 1982; Bessell & Brett 1988). Since the average disk dissipation timescale for T Tauri stars is 3×10^6 years (Strom *et al.* 1989), we assumed that objects older than 10^7 years are unlikely to possess disks that would produce excess emission at K. Therefore, stars falling below the reddening line for a 0.1 $M_\odot$ star of 10^7 years old (bottom dashed line) are either association members too old to possess disks or field stars. As a result, we find 184 objects in this regime that have a complete set of JHK magnitudes and can be used to define the slope of the reddening line in the color-color diagram. We have assumed that brown dwarfs in the cloud comprise

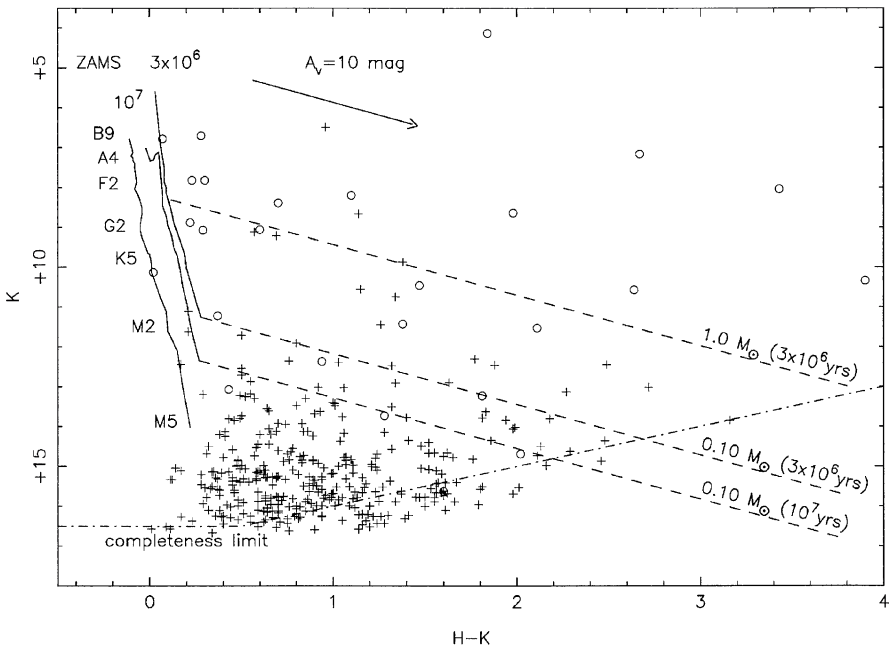

FIG. 5. A color-magnitude diagram showing the distribution of objects relative to the ZAMS and to 10^7 year and 3×10^6 year isochrones for stars with masses from 0.1 to 2.5 $M_\odot$ assuming a distance of 130 pc. The isochrones were determined using the models of D'Antona & Mazzitelli (1994). The ZAMS has been offset to the left by 0.1 mag in $(H-K)$ for presentation purposes. Open circles represent 21 known association members plus 5 brown dwarf candidates. Sources marked with plus signs are either candidate association members or field stars. The reddening vector for $A_v=10$ mag is derived from the reddening law for the Ophiuchus cloud (Elias 1978) transformed from the CIT system to the Bessell & Brett system: $A_v=11.55\,E(H-K)$ or $A_K=1.27\,E(H-K)$. The reddening lines are shown for stars of masses 0.1 $M_\odot$ for 10^7 years and 3×10^6 years and for 1.0 $M_\odot$ for an age of 3×10^6 years. We note that the actual slope of the reddening lines appropriate to the R Cr A cloud may differ slightly from that in Ophiuchus but our conclusions are not sensitive to the precise value. Conclusions drawn from color-magnitude diagrams constructed with reddening laws based on both standard reddening [$A_K=1.78\,E(H-K)$; Wilking *et al.* 1994] and the Ophiuchus cloud reddening are very similar.

an insignificant fraction of objects below the reddening line with a complete set JHK magnitudes; if such cool and faint objects did exist, they would not likely be detected at J.

A $(J-H)$ vs $(H-K)$ diagram for the diskless sample is shown in Fig. 6(a) and contains stars reddened by 0–20 mag of visual extinction. The intrinsic colors for main sequence and giant stars are shown as solid lines and were taken from Bessell & Brett (1988). The band for main sequence and giant stars reddened by interstellar dust is delineated by dashed lines and has a slope defined by this sample of $(J-H)/(H-K)=1.5\pm0.05$. This slope is also consistent with the locations of 5 sources which have been observed to have no excess at $\lambda=3.4$ μm (IRS 4, IRS 10, IRS 14, IRS 15, VSS 7; Wilking *et al.* 1986) and with stars identified spectroscopically as background giants (VSS 7, IRS 4, 185800.6-370056, 185903.8-371005; Wilking & Meyer 1997). As shown in Fig. 6(a), the slope of 1.5 gives a shallower reddening vector compared to the value of 1.95 derived for normal interstellar dust (Bessell & Brett 1988). This value is also less than the value of 1.69 found for the ρ Oph cloud transformed into the Bessell & Brett system (Elias 1978). The shallower slope observed for the R Cr A cloud is predicted qualitatively by models if the region has larger than average grain sizes (Steenman & Thé 1989). Indeed, photometric studies suggest a larger than average value of R for the cloud indicative of grain growth ($R=4.4\pm0.8$, Vrba & Rydgren 1984).

3.3.2 Color-color diagram and disk frequency

The sample of objects *above* the reddening line for a 0.1 $M_\odot$ star of 10^7 years constitutes a sample of potential association members but may also contain luminous background stars. These 51 sources are plotted in the color-color diagram in Fig. 6(b) with the 19 known association members plus Star A denoted by open circles.[3] Using the slope for the reddening band determined from the diskless sample, only 8 of the 51 sources are offset by 0.1 mag or more from the band and hence show evidence for K band emission from circumstellar disks. Five of these 8 are among the known association members in the diagram. The excess sources include (in order of decreasing $(J-H)$): HH 100-IR, IRS 5, IRS 9, R Cr A, IRS 3(new), 185853.3-370328(new), T CrA, and 185815.3-370435(new). The source 185853.3-370328 is extended in our images and may be an unresolved double. Assuming the new excess sources are association members, the resulting disk frequency ranges from 16% (8 of 51) to 35% (8 of 23), depending on whether all or none of the 28

[3]Known association members from Tables 1 and 2 in this diagram include emission-line stars, x-ray sources, and sources with infrared excesses at $\lambda=3.4$ to 100 μm: R Cr A, TY Cr A, HD 176386a, IRS 2, T Cr A, HH 100-IR, Hα 2, GP wa, IRS 5, IRS 6, IRS 13, IRS 9, IRS 8, IRS 11, VSS 13, Hα 14, GP e2, and 185805.9-370356 (x-ray source). GP wb has been identified spectroscopically as a pre-main-sequence star by Wilking & Meyer (1997). We have plotted the Hα emission-line object Star A (Graham 1993) as an association member even though it falls below the reddening line.

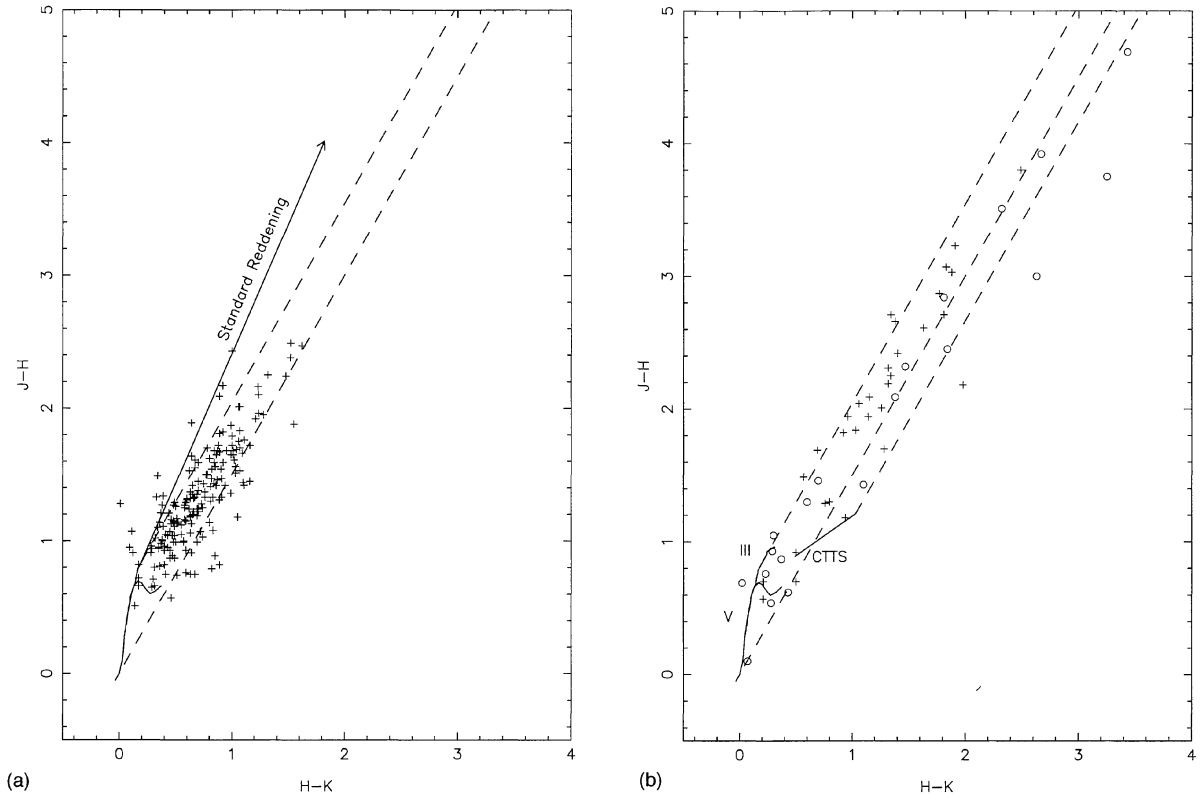

FIG. 6. Color-color diagrams for (a) stars unlikely to have circumstellar disks, and (b) possible association members. All data are in the system of Bessell & Brett (1988). The slope of the reddening lines, $(J-H)/(H-K)=1.5$, is defined by the sample in (a). In (a), the objects plotted are those that fall below the reddening line for a 0.1 $M_\odot$ star with an age of 10^7 years. The loci of unreddened dwarf and giant stars are shown by the solid lines. The reddening vector for a standard reddening law is shown for comparison (Bessell & Brett 1988). In (b), the objects plotted are those the lie above the reddening line for a 0.1 $M_\odot$ star with an age of 10^7 years. In addition to the loci of unreddened dwarfs (V) and giants (III), the loci of unreddened classical T Tauri stars (CTTS) is also shown as determined by the study of Meyer *et al.* (1997) and transformed into the Bessell & Brett system. The open circles represent 19 known association members plus a possible substellar object, Star A.

unclassified sources in the diagram are actual association members. We note that the blind adoption of a standard slope of 1.95 would have created 24 false excess sources. This disk frequency is much lower than that found at L ($\lambda=3.4$ μm) by Wilking *et al.* (1986); of the 12 association members they found with L band excesses, only 5 have K band excesses in this study.

The color-color diagram may also be used to infer the evolutionary states of YSOs. Classical T Tauri stars (Class II sources) form a locus of unreddened stars shown in Fig. 6(b) that is above and to the right of unreddened dwarfs and giants (Lada & Adams 1992; Meyer *et al.* 1997). The more deeply embedded Class I sources are found to the right of the Class II reddening band. Based on their locations in the diagram, the sources HH 100-IR, IRS 5, IRS 9, and IRS 3 are Class I YSOs. IRS 2, R Cr A, T Cr A, 185853.3-370328, and 185815.3-370435 fall in the regime of reddened classical T Tauri stars, as do known association members just inside the main sequence reddening band: IRS 6, IRS 11, IRS 13, and IRS 8. Except for IRS 2 and T Cr A, these evolutionary classifications are consistent with those determined from spectral energy distributions (SEDs) constructed from ground-based near-to-mid infrared data as well as data from the KAO and *IRAS* (Wilking *et al.* 1986; Wilking *et al.* 1992). IRS 2 has a Class I SED (1.2-60 μm) and T Cr A has a double-peaked spectrum (0.36–20 μm) characteristic of a Class I source with holes in its dusty envelope (Calvet *et al.* 1994). Extensive infrared reflection nebulae observed toward IRS 2 and T Cr A (as well as R Cr A, IRS 6, IRS 5, and HH 100-IR, see Fig. 2), could distort the positions of these stars in the diagram and their subsequent classification (Kenyon *et al.* 1993).

3.4 Color-Magnitude Diagram: A YSO Census

Given the low number of infrared excess sources, we can use the K vs $(H-K)$ diagram in Fig. 5 to gain insight into the maximum number of low-luminosity YSOs in our mosaic. For this discussion, we will use the 3×10^6 year isochrone and the middle dashed line which marks the reddening line for 0.10 $M_\odot$ objects at this age. Given these assumptions and the completeness limits of our survey, our diagram is complete for all low-luminosity YSOs in the cloud ($M>0.1$ $M_\odot$) to a depth of $A_v=30$ mag. Hence, our infrared survey has completely sampled all YSOs throughout about 80% of the depth of the cloud core.

Among the 365 stars plotted in this diagram, 21 are identified as association members plus five brown dwarf candi-

dates (open circles).[4] A total of 39 sources lie above the reddening line for a 0.1 $M_\odot$ star of age 3×10^6 years with 21 of these known to be associated with the cloud. Therefore, 18 of the stars above the reddening line for a 0.1 $M_\odot$ star have not been classified and could either be association members without K band excesses or field stars. Infrared spectroscopy, observations in the thermal infrared, or x-ray observations are needed to determine the nature of these sources. Given their locations at the edges of the cloud core, many of these are probably luminous, background field stars.

As shown in Fig. 5, there are 5 proposed association members which lie below the reddening line for a 0.1 $M_\odot$ star and hence are brown dwarf candidates: nebulous objects 185839.6-365823 and 185840.4-370433, the emission-line star Star A (Graham 1993), and the new K band excess sources 185815.3-370435 and 185853.3-370328 (see Table 1). We note that it is possible that these objects are not substellar but rather association members older than 3×10^6 years old, association members displaced below the 0.1 $M_\odot$ reddening line due to presence of scattered light (Kenyon *et al.* 1993), unresolved binaries, or unusual background objects. Further study is warranted to determine their true natures.

4. IMPLICATIONS FOR CLUSTER FORMATION

The R Cr A infrared cluster contained within our mosaic contains at least 22 association members (including IRS 7) and could comprise as many as 40 members total. An additional 5 proposed association members appear in the substellar regime and are in need of further observations. This estimate of 22-40 YSOs does not include 13 known association members outside of our field of study that have been identified as YSOs through *IRAS* observations of the Corona Australis cloud complex (Wilking *et al.* 1992). The 10 YSOs within 0.11 pc of (and including) the star R Cr A, which comprise the Coronet cluster, appear to have formed nearly simultaneously. Our images reveal nebulosity associated with seven of these objects, indicative of extensive circumstellar dust. Included in this group is IRS 7, whose near-infrared emission is due entirely to scattered light. In addition, the YSOs IRS 3 and IRS 9 have strong infrared excesses at K and L, and the latter source has been identified as the probable exciting star for the HH 99 system.

As noted by Taylor & Storey (1984), the YSOs in the core of the R Cr A cloud are centrally condensed; 13 of the 22 confirmed YSOs are contained within a projected radius of 0.15 pc of the star R Cr A and 10 YSOs within 0.11 pc. The resulting stellar densities are 920 stars pc^{-3} and 1950 stars pc^{-3}, respectively, assuming a spherical geometry for the cluster. These stellar densities are not strongly affected by incompleteness due to intracloud extinction since our survey has completely sampled YSOs through most of the cloud core. The morphology and stellar density of the Coronet cluster are common to other embedded clusters such as those associated with NGC 2024, NGC 2068, and NGC 2071 in Orion (Lada *et al.* 1991) and BD+40° 4124 (Hillenbrand *et al.* 1995). In other words, these clusters contain a luminous visible star with an attendant cluster of lower mass stars embedded in a dense molecular core. The stellar densities in the Orion clusters range from 440 – 4000 stars pc^{-3} and the density in BD+40° 4124 is estimated to be at least 1840 stars pc^{-3} if one assumes a spherical geometry.

Although there are relatively fewer YSOs in the Coronet cluster, the stellar density is high enough that, like these richer clusters, the stars cannot be considered to have formed in isolation. There are several lines of evidence that YSOs in the Coronet may have affected the formation of their neighbors. First, the mean separation of stars within 0.11 pc of the star R Cr A is 0.1 pc (20,000 AU), which is comparable to the diameter of an isolated molecular core forming a single star (Myers & Benson 1983; Benson & Myers 1989). Second, dust-free cavities adjacent to HH 100-IR and IRS 2 suggest that winds from these stars have swept out areas 0.03–0.05 pc in diameter (6000–10,000 AU). Finally, the proposed association of HH 99 with a source near the cluster center implies that its wind is impacting the ambient cloud at a projected distance of 0.1 pc from the YSO.

5. SUMMARY

We have obtained deep J, H, and K' images of a 170 square arcminute area of the R Cr A molecular cloud core. Completeness limits of 17.5, 17.0, and 16.5 mag were achieved at J, H, and K'. Accurate positions and near-infrared magnitudes have been determined for 692 sources; this information is presented for 125 sources with $K'<15$ mag. We estimate that our broad-band survey has completely sampled association members with $M>0.1$ $M_\odot$ through about 80% of the depth of the molecular core. Our images afford a closer look at the Coronet cluster, revealing infrared reflection or HH nebulae associated with most of these YSOs. This suggests nearly simultaneous star formation within this high stellar density region. Our data reveal that the most deeply embedded cluster member (IRS 7), which lies at the center of the strongest emission from cold dust and dense gas, is not a point source at K'. The true position of IRS 7 has been determined from 10 μm imaging to be 3″ northwest of the K' source and is within 1″ of the radio continuum VLA source IRS 7A.

Narrow-band images have defined regions of shocked molecular gas and high excitation atomic gas in HH 99 and HH 104C&D. HH 99B possesses a jet/bow shock morphology; the head of the bow shock and jet are defined by [Fe II] emission, trailed by a wake delineated by H_2 emission. The orientation of the proposed jet and wake suggests that IRS 9 is the most likely excitation source. The structure of HH 99A is that of an ambient clump caught up in the same outflow. A new, filamentary HH object east of HH 99A&B may be a

[4]In addition to the 19 association members in the color-color diagram, we have added the new K band excess source IRS 3 and HD 176386b. HD 176386b has been identified spectroscopically as a pre-main sequence star by Wilking & Meyer (1997). The brown dwarf candidates which fall below the reddening line for a 0.1 $M_\odot$ star at 3×10^6 years include Star A, two of the new excess sources (185853.3-370328 and 185815.3-370435), and two star-like objects surrounded by low-level nebulosity (185839.6-365823 and 185840.4-370433). Association member IRS 7 is excluded from the diagram since its near-infrared magnitudes are primarily from scattered light.

remnant of a previous episode of ejection or mass loss from IRS 9. Discrete knots of [Fe II] and H_2 emission have been found coincident with HH 104C&D. Several lower excitation knots seen in H_2 only are found northeast of C&D and suggest that the excitation of the system involves IRS 5 and/or IRS 6, rather than the star R Cr A as previously suggested.

Infrared color-color and color-magnitude diagrams have been used to determine the natures of the sources revealed though broad-band imaging. The vast majority of the sources are field stars. We have taken advantage of this fact and used the field stars to calibrate the slope of the reddening band in the $J-H$ vs $H-K$ diagram to an $A_v=20$ mag. We find that the derived slope of $(J-H)/(H-K)=1.5\pm0.05$ is much shallower than that given by a standard reddening law, but consistent with the presence of larger than average dust grains in the cloud. Using this derived slope, only 8 objects are observed with infrared excesses at K which sets the disk frequency in the range of 16% to 35%. Assuming a common age for the cluster of 3×10^6 years, we identify between 22 and 40 association members in our sample. In addition, there are five brown dwarf candidates. The resulting stellar density within a 0.1 pc radius of the star R Cr A is about 2000 stars pc^{-3}, similar to that found for embedded clusters with ~100 stars or less. Even in this relatively sparse cluster, it is expected that YSOs have had an influence on the formation and evolution of their neighbors.

We are most grateful to Michael Meyer for many fruitful discussion and critical comments. We thank Darren Hale who assisted with the reduction of these data and Michael Kunkel who obtained and reduced the ESO photometry. H.Z. thanks U. Käufl for his invaluable assistance with the TIMMI observations. Thanks also go to Burt Jones who provided us with a list of astrometric reference stars. H.Z. and B.W. acknowledge support from NATO Grant No. CRG 910174 and B. W. gratefully acknowledges RUI Grant No. NSF AST-9417210 to the University of Missouri–St. Louis.

APPENDIX A. TRANSFORMATIONS TO THE PHOTOMETRIC SYSTEM OF BESSELL & BRETT

It was desirable to place the photometry obtained with different telescopes into a standard photometric system. This facilitates the combination of these data in uniform color-color and color-magnitude diagrams. It also aids in comparison with reddening laws, intrinsic colors for main sequence stars, and theoretical models for PMS evolution. For ease of comparison, the system of Bessell & Brett (1988) was chosen.

The data from the imaging survey presented in Table 1 is in the natural system of the NICMOS3 camera. The first step in transforming the NICMOS3 photometry was to use color equations derived to move the array data to the IRTF system (RC1 InSb system) and to move the K' photometry into the standard K band. For this, we used the prescription determined by Rayner (1997):

$$K_{\rm irtf}=K'_{\rm nicmos}-0.08(H-K')_{\rm nicmos}, \quad \text{(A1)}$$

$$(H-K)_{\rm irtf}=1.15(H-K')_{\rm nicmos}, \quad \text{(A2)}$$

$$(J-H)_{\rm irtf}=(J-H)_{\rm nicmos}+0.13(H-K')_{\rm nicmos}. \quad \text{(A3)}$$

The data could not be transformed directly from the IRTF system into the Bessell & Brett system. An intermediate step was needed that used the equations derived by Humphreys *et al.* (1984) to go from the IRTF to the CIT system (Elias *et al.* 1982). From there, the relations derived between the CIT system and the system of Bessell & Brett by the latter could be used. The full transformation from the NICMOS3 data to the Bessell & Brett system is then:

$$K=K_{\rm CIT}=K_{\rm irtf}, \quad \text{(A4)}$$

$$(H-K)=1.24(H-K')_{\rm nicmos}, \quad \text{(A5)}$$

$$(J-H)=0.93(J-H)_{\rm nicmos}+0.12(H-K')_{\rm nicmos}. \quad \text{(A6)}$$

Photometry presented in Table 2 obtained from the SAAO (Glass & Penston 1975), and AAO (Taylor & Storey 1984) were placed into the Bessell & Brett (1988) system using the prescriptions given by the latter. Since a recent paper by Bouchet *et al.* (1991) provides a better characterization of the ESO photometric system and demonstrates the similarity between the ESO and SAAO photometric systems, the ESO data in Table 2 were transformed into the Bessell & Brett system using their equations for SAAO data. No transformations were applied to ProtoCAM photometry for the star HD 176386b. However, we note that the star is unreddened and color transformations are not necessary.

APPENDIX B. BINARIES IN THE R CR A CLOUD

There are several complete samples of young objects one can consider to explore the binary fraction in this cloud. First is the sample defined by our near-infrared observations which is complete for binaries with components $M>0.1\ M_\odot$ for ages less than 3×10^6 years and projected separations greater than 1″ through most of the depth of the cloud. But among the 27 association members and brown dwarf candidates identified by this study, only 2 binaries were identified with projected separations of between 1-8″(130-1040 AU). Both are visual pairs: HD 176386a&b (sep.=3.7″) and GP wa&b (sep.=4.6″). The pre-main-sequence nature of the secondaries has been confirmed by infrared spectroscopy (Wilking & Meyer 1997). We note there are two additional stars in our survey known to be multiple but our observations could not resolve these or similar systems: TY Cr A is an eclipsing triple system (Casey *et al.* 1993) and IRS 5(TS 2.4) is double with a projected separation of 0.6″ (Chen & Graham 1993). Given 2 binaries among 20 systems associated with the cloud (excluding brown dwarf candidates), a binary frequency of $10.0\%\pm7.1\%$ is implied. For comparison, this binary fraction is consistent with the value of 7.8% computed for G dwarf stars over the corresponding range of periods (Duquennoy & Mayor 1991), although our sample is small and the uncertainties large.

A second sample is that observed by *IRAS* and includes both embedded sources, classical T Tauri stars, and early-

type stars associated with the cloud. This sample is complete for objects throughout the depth of the cloud with $L > 1\ L_{\odot}$. Among this sample of 23 young objects are four systems: the aforementioned HD 176386a&b, VV Cr A (1.9″, Graham 1992), S Cr A (1.3″, Joy & van Biesbrock 1944), and the double B8 stars SAO 210815/SAO 210816 (13″). The latter is listed in the Bright Star Catalogue as a common proper motion pair with one member as a spectroscopic binary. But it is not certain that they comprise a gravitationally bound system. The resulting binary fraction is $17\% \pm 8.7\%$ including the double B8 system and $13\% \pm 7.5\%$ excluding the latter system.

Finally, a recent study of *Einstein* x-ray observations of the cloud by Walter *et al.* (1997) reveal a close pair corresponding to Hα 11 (sep.=3″) and a very wide pair (CrAPMS 4, sep.=43″). In addition, x-ray emission was detected from the aforementioned GP w, TY Cr A, and SAO 210815/SAO 210816 systems. If all are gravitationally bound systems, an x-ray binary fraction of $45\% \pm 20\%$ is implied. Considering projected separations similar to the near-infrared selected sample (1″–8″), the binary fraction would be $18\% \pm 13\%$ which is consistent with that of the *IRAS* and near-infrared selected samples given their large mutual uncertainties.

REFERENCES

Allen, D. A., *et al.* 1993, Proc. Astron. Soc. Aust., 10, 298
Allen, D. A., & Burton, M. G. 1993, Nature, 363, 54
Benson, P. J., & Myers, P. C. 1989, ApJS, 71, 89
Bessell, M. S., & Brett, J. M. 1988, PASP, 100, 1134
Bouchet, P., Manfroid, J., & Schmider, F. X. 1991, A&AS, 91, 409
Brown, A. 1987, ApJ, 322, L31
Calvet, N., Hartmann, L., Kenyon. S., & Whitney, B. 1994, ApJ, 434, 330
Carpenter, J. M., Snell, R. L., Schloerb, F. P., & Skrutskie, M. F. 1993, ApJ, 407, 657
Casey, B. W., Mathieu, R., Suntzeff, N. B., Lee, C-W., & Cardelli, J. A. 1993, AJ, 105, 2276
Castelaz, M. W., & Hackwell, J. A. 1987, ApJ, 314, 317
Chen, W. P., & Graham, J. A. 1993, ApJ, 409, 319
Cohen, M., Schwartz, R. D., Harvey, P. M., & Wilking, B. A. 1984, ApJ, 281, 250
D'Antona, F., & Mazzitelli, I. 1994, ApJS, 90, 647
Duquennoy, A., & Mayor, M. 1991, A&A, 248, 485
Elias, J. H. 1978, ApJ, 224, 453
Elias, J. H., Frogel, J. A., Matthews, K., & Neugebauer, G. 1982, AJ, 87, 1029
Glass, I. S., & Penston, M. V. 1975, MNRAS, 172, 227
Graham, J. A. 1992, PASP, 104, 479
Graham, J. 1993, PASP, 105, 561
Harju, J., Haikala, L., Mattila, K., Mauersberger, R., Booth, R., & Nordh, H. 1993, A&A, 278, 569
Henning, Th., Launhardt, R., Steinacker, J., & Thamm, E. 1994, A&A, 291, 546
Herbig, G. H., & Bell, K. R. 1988, Lick Obs. Bull., No. 1111
Hezel, T., Wilking, B., Mundy, L., & McMullin, J. 1994 (unpublished)
Hillenbrand, L. A., Meyer, M. R., Strom, S. E., & Skrutskie, M. F. 1995, AJ, 109, 280
Hodapp, K.-W., & Rayner, J. 1991, AJ, 102, 1108
Hodapp, K.-W., Rayner, J., & Irwin, E. 1992, PASP, 104, 441
Howell, S. B. 1989, PASP, 101, 612
Humphreys, R. M., Jones, T. J., & Sitko, M. L. 1984, AJ, 89, 1155
Joy, A. H., & van Biesbrock, G. 1944, PASP, 56, 123
Kenyon, S. J., Whitney, B. A., Gomez, M., & Hartmann, L. 1993, ApJ, 414, 773
Knacke, R. F., Strom, K. M., Strom, S. E., & Kunkel, W. E. 1973, ApJ, 179, 847
Lada, C. J., & Adams, F. C. 1992, ApJ, 393, 278
Lada, E. A., DePoy, D. L., Evans II, N. J., & Gatley, I. 1991, ApJ, 371, 171
Levreault, R. M. 1988, ApJS, 67, 283
Loren, R. B., Sandqvist, A., & Wootten, H. A. 1983, ApJ, 270, 620
Marraco, H. G., & Rydgren, A. E. 1981, AJ, 86, 62
McCaughrean, M., & Stauffer, J. R. 1994, AJ, 108, 1382
Meyer, M. R., Calvet, N., & Hillenbrand, L. A. 1997, AJ, 114, 288
Myers, P. C., & Benson, P. J. 1983, ApJ, 266, 309
Patten, B. 1994, private communication
Rayner, J., Hodapp, K.-W., & Zinnecker, H. 1991, in Astrophysics with Infrared Arrays, ASP Conf. Ser. 14, edited by R. Elston (ASP, San Francisco), p. 264
Rayner, J. 1997, in preparation
Saraceno, P., André, P. Ceccarelli, C., Griffin, M., & Molinari, S. 1996, A&A, 309, 827
Schmidt-Kaler, Th. 1982, in Landolt-Bornstein New Series, Numerical Data and Functional Relationships in Science and Technology, Group 4, Vol. 2b, edited by K. Schaffers and H. H. Voigt (Springer, New York), p. 451
Steenman, H., & Thé, P. S. 1989, Ap&SS, 159, 189
Strom, K., Strom, S., Edwards, S., Cabrit, S., & Skrutskie, M. 1989, AJ, 97, 1451
Taylor, K. N. R., & Storey, J. W. V. 1984, MNRAS, 209, 5P
Vrba, F. J., & Rydgren, A. E. 1984, ApJ, 283, 123
Vrba, F. J., Strom, S. E., & Strom, K. M. 1976, AJ, 81, 317
Wainscoat, R. J., & Cowie, L. L. 1992, AJ, 103, 332
Walter, F. M. 1986, ApJ, 306, 573
Walter, F. M., Vrba, F. J., Wolk, S. J., Mathieu, R. D., & Neuhäuser, R. 1997, AJ, 114, 1544
Wilking, B., Greene, T., Lada, C., Meyer, M., & Young, E. 1992, ApJ, 397, 520
Wilking, B., Giblin, T., McCaughrean, M., Rayner, J., Burton, M., & Zinnecker, H. 1994, in Infrared Astronomy with Arrays: The Next Generation, edited by I. McLean (Kluwer, Dordrecht), p. 17
Wilking, B. A., & Lada, C. J. 1983, ApJ, 274, 698
Wilking, B. A., & Meyer, M. R. 1997, in preparation
Wilking, B. A., Schwartz, R. D., Mundy, L. G., & Schultz, A. S. B. 1990, AJ, 99, 344
Wilking. B. A., Taylor, K. N. R., & Storey, J. W. V. 1986, AJ, 92, 103
Zinnecker, H., McCaughrean, M., & Wilking, B. 1993, in Protostars and Planets III, edited by E. Levy and J. Lunine (Arizona Press, Tucson), p. 429

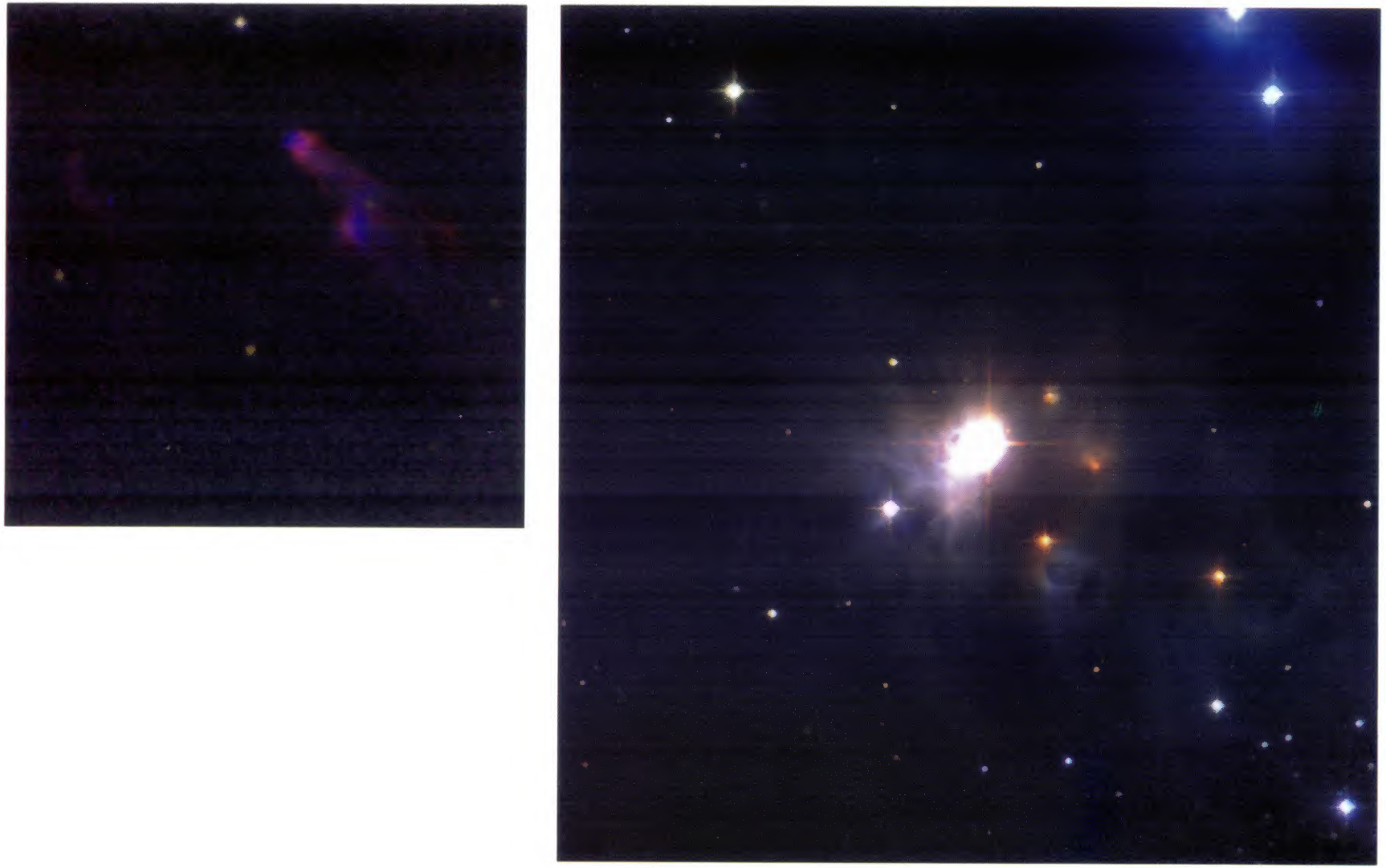

FIG. 2. Three-color composite images of the central region of the *JHK′* survey and a smaller image covering the HH 99 region. On the right, a composite *JHK′* image of the central 8.6×9.1 arcmin of the R Cr A cloud core is shown. The broad-band *J*, *H*, and *K′* images have been coded with colors blue, green, and red, respectively. Centered in the image is the emission-line star R Cr A; additional objects are identified in Fig. 3. Note that HH 99A&B are apparent, northeast of the star R Cr A. On the left, an emission-line composite image of the HH 99 region is shown. The image covers a 1.8×1.8 arcmin region. [Fe II] (1.644 μm) emission is coded in blue, Br γ (2.166 μm) in green, and H_2 (2.12 μm) in red. Note that the [Fe II] emission in HH 99B (north-east) forms a cap on the bow shock delineated by H_2 emission. In HH 99A (south-west of B), the [Fe II] emission is shifted to the west of the H_2 emission suggesting that it is a shocked ambient clump.

Wilking *et al.* (see page 2034)